Enhanced thermoelectric performance and high-temperature thermal stability of *p*-type Ag-doped β-Zn_4Sb_3

Lirong Song[a], Anders B. Blichfeld[b], Jiawei Zhang[a], Hidetaka Kasai[c], and Bo B. Iversen[a,*]

[a]*Center for Materials Crystallography, Department of Chemistry and iNANO, Aarhus University, DK-8000 Aarhus, Denmark*

[b]*Department of Materials Science and Engineering, NTNU Norwegian University of Science and Technology, NO-7491 Trondheim, Norway*

[c]*Faculty of Pure and Applied Sciences, Tsukuba Research Center for Energy Materials Science (TREMS), University of Tsukuba, 1-1-1 Tennodai, Tsukuba, Ibaraki, 305-8571, Japan*

[*]Corresponding author. E-mail address: bo@chem.au.dk

Abstract

Here we report that the thermoelectric properties of bulk β-Zn_4Sb_3 at 300 - 575 K can be improved by doping Ag at the Zn sites. Proper Ag doping leads to decreased electrical resistivity and increased Seebeck coefficient, thus resulting in a large improvement in power factor. The figure of merit, *zT*, has an obvious enhancement due to Ag doping although the thermal conductivity is slightly increased. $(Zn_{0.9925}Ag_{0.0075})_4Sb_3$ exhibits a promising *zT* of ~1.2 at 575 K, which is superior to most previously reported p-type doped Zn_4Sb_3 materials. Furthermore, the high-temperature thermal stability is studied in details. The $(Zn_{0.9925}Ag_{0.0075})_4Sb_3$ bulk sample does not decompose even when the temperature is elevated to 793 K in vacuum. When the bulk sample is heated to 573 K in air, $(Zn_{0.9925}Ag_{0.0075})_4Sb_3$ is also stable, but Zn whiskers come out of the surface for undoped Zn_4Sb_3. In-house in situ powder X-ray diffraction (PXRD) and multi-temperature synchrotron PXRD (up to 793 K) reveal that the undoped Zn_4Sb_3 powder sample starts decomposing into ZnSb at 473 K if exposed to the air and it is fully decomposed into ZnSb, ZnO, and Sb after cooling down from 793 to 300 K. However, there is ~24 wt% Zn_4Sb_3 preserved in the $(Zn_{0.995}Ag_{0.005})_4Sb_3$ powder sample after the same heat treatment, while only ~6 wt% Zn_4Sb_3 remains in $(Zn_{0.99}Ag_{0.01})_4Sb_3$. The above result indicates that proper Ag doping leads to enhanced high-temperature thermal stability in β-Zn_4Sb_3. This work thereby demonstrates Ag-doped Zn_4Sb_3 bulk material as a promising candidate for thermoelectric material in terms of enhanced performance as well as improved high-temperature thermal stability.

1. Introduction

In recent decades, enormous attentions have been paid to thermoelectric materials because of their potential applications in waste-heat recovery, power generation, and refrigeration through solid state devices without moving parts. The performance of thermoelectric materials is evaluated via the dimensionless figure of merit, $zT = S^2\sigma T/\kappa$, where *S* is the Seebeck coefficient, σ the electrical resistivity, *T* the absolute temperature and κ the thermal conductivity. β-Zn_4Sb_3 is an intriguing thermoelectric material in the intermediate temperature range (400 - 700 K) and a promising candidate to substitute Pb-Te alloys, due to its excellent TE performance as well as nontoxic, earth-abundant and cheap chemical elements [1]. Four crystallographic phases of Zn_4Sb_3 have been reported so far, which are the α'-phase (below 230 K), α-phase (230 - 263 K),

β-phase (263 - 765 K) and γ-phase (from 765 K to the melting point 837 K) [2, 3]. Among these phases, only the β-phase exhibits high thermoelectric properties with the largest reported *zT* value of 1.3 at 673 K [1], originating from its remarkable "phonon-glass" nature. The glass-like low thermal conductivity in β-Zn_4Sb_3 is mainly attributed to the complex crystal structure, including the Zn disorder and the interstitial Zn sites [4, 5]. It also has been found that the very low thermal conductivity of Zn_4Sb_3 is intrinsic to the structure and can be due to the anharmonic motion of the Sb1 atoms coordinated only by Zn atoms [6].

Although β-Zn_4Sb_3 is known as a good thermoelectric material, the thermoelectric performance needs to be further improved for the final industrial application. Up to date, the *zT* value of β-Zn_4Sb_3 has been enhanced through many approaches, such as developing new synthesis methods [7], elemental doping and nano-structuring [8]. The traditional strategy of doping has been widely explored to improve the TE properties by tuning the carrier concentration to optimize the power factor ($S^2\sigma$). Dopants, such as Cd [9], Al [10], Ga [10], In [10, 11], Hg [12], Nb [13], Te [14, 15], Mg [16, 17], Ag [18, 19], Cu [18], I [20], Se [21], Fe [22], Bi [23], and Pb [24], have been investigated in β-Zn_4Sb_3 so far. However, most of the above investigations (including Ag doping) were done below room temperature. Since β-Zn_4Sb_3 displays good TE performance above 473 K, it is vital to explore the doping effects at high temperatures as well. To our best knowledge, a systematic study of Ag doping effects on the thermoelectric performance above room-temperature of β-Zn_4Sb_3 has not yet been reported.

In spite of the superior thermoelectric performance at intermediate temperatures in β-Zn_4Sb_3, thermal stability has been problematic in its commercial application [3, 25-29]. The decomposition could even happen at a temperature much lower than the β-γ phase transition point (765 K). Here it is imperative to study the thermal stability of β-Zn_4Sb_3 phase. Therefore, in this work we focus on the effects of Ag doping on thermoelectric properties of β-Zn_4Sb_3 as well as the high-temperature thermal stability by X-ray diffraction measurements (In-house in situ and multi-temperature synchrotron PXRD) and differential thermal analysis (DTA).

2. Experimental section

2.1 Synthesis

$(Zn_{1-x}Ag_x)_4Sb_3$ (x = 0, 0.005, 0.0075, 0.01 and 0.015) compounds were synthesized by the fast and effective spark plasma sintering (SPS) method. The high-purity elements zinc (powder, 99.99%, Merck KGaA), antimony (powder, 99.5%, Sigma-Aldrich Chemie GmbH), and silver (powder, 99.99%, Sigma-Aldrich Chemie GmbH) were weighed according to the stoichiometric ratio and mixed in a ball mill mixer (SpectroMill, CHEMPLEX INDUSTRIES, INC) for 15 min. Then the mixed powders were loaded into a 12.7 mm diameter graphite die protected by BN spray at both the top and bottom side of the punches. Meanwhile, a Zn round foil (thickness of 0.15 mm; purity 99.95+%) with the same diameter as the die was placed at the bottom side between powders and BN spray so as to compensate the loss of Zn composition during the synthesis [29]. The powders were compacted and sintered by spark plasma sintering (SPS) under a pressure of 100 MPa by an SPS-515 instrument (SPS SYNTEX INC, Japan). SPS sintering was performed in vacuum by heating to 673 K in 10 min and staying for 5 min. Thereafter the power was turned off and the pressure was released slowly. PXRD patterns of all as-pressed pellets were characterized before property measurements up to 573 K. After all the property measurements each of the five pellets was characterized by XRD again and then cut into two halves for Potential Seebeck Microprobe

(PSM) scanning. According to the same experimental synthesis method described above, we made three more pellets (x = 0, 0.005, and 0.01), which were ground into powders for the measurements of in-house in situ PXRD, DTA and multi-temperature synchrotron PXRD.

2.2 In-house X-ray diffraction and synchrotron powder X-ray diffraction

Both the top and bottom sides of the as-prepared $(Zn_{1-x}Ag_x)_4Sb_3$ pellets were characterized by X-ray diffraction measurements with a Cu $K\alpha_1$ radiation source (wavelength: 1.54056 Å) and Bragg-Brentano beam optic on the Rigaku Smartlab diffractometer. The X-ray diffraction measurements were also carried out on the top sides of the pellets after all the high-temperature property measurements.

In-house in situ PXRD measurements (the wavelength: 1.78892 Å) were done for the Zn_4Sb_3 powders which were obtained from the as-pressed Zn_4Sb_3 pellet. The powders were packed densely in the sample holder and then carefully placed on the Anton Paar DHS 1100 domed heating stage. The measurements were performed in air. The temperature program was heating the sample from room temperature to 698 K at a rate of 10 K/min, continuing heating up to 773 K at a slower rate of 1 K/min and staying at this temperature for 1 h. Later the temperature was lowered to 698 K at the rate of 1 K/min and continued cooling down to 313 K at the rate of 10 K/min. The diffraction patterns were collected in a narrow scattering angle (2θ) range of 20 - 60°. Each scan takes approximately 3 min, thus the temperature actually changes ~ 3 K from the start til the end of each scan when the heating/cooling rate is 1 K/min. ~ 1 min is needed for coming back to the start of a new scan.

In-house in situ XRD measurements were also performed for the pellet $(Zn_{1-x}Ag_x)_4Sb_3$ (x = 0.0075) after the property measurements, where the top side was put upwards on the heating stage. One half of the pellet $(Zn_{0.9925}Ag_{0.0075})_4Sb_3$ was heated in vacuum from room temperature to 573 K and cooled down to 301 K at the rate of 2 K/min in the first cycle, and heated up to 573 K at the rate of 20 K/min and cooled down to 301 K in the second cycle. In the third cycle, the sample was heated to 793 K and cooled to 308 K at the rate of 30 K/min. The XRD data were collected at 301, 573 and 301 K in the first cycle, at 573 and 301 K in the second cycle, and at 773, 793 and 308 K in the last cycle. Each XRD pattern takes approximately 47 min in the 2θ range of 20 - 110°. The other half of the pellet $(Zn_{0.9925}Ag_{0.0075})_4Sb_3$ and one half of the pellet Zn_4Sb_3 were both heated in air from room temperature to 573 K and then cooled down in the rate of 2 K/min. XRD data were collected at 300 K before heating, 573 K and 300 K after cooling. It takes 104 min for each XRD pattern.

Multi-temperature synchrotron PXRD data were collected at the SPring-8 BL02B2 [30] and BL44B2 beamline [31] for the three samples $(Zn_{1-x}Ag_x)_4Sb_3$ (x = 0, 0.005 and 0.01). The powders were floated and packed in air in 0.2 mm quartz capillaries which were sealed in air. The heating rate is 50 K/min between each fixed temperature with an exposure time of 15 min. The wavelength was calibrated to λ = 0.49814(1) Å (BL02B2) and λ = 0.500456(2) Å (BL44B2) using a CeO_2 standard. The data were collected at 300, 773 and 793 K on heating as well as at 773 and 300 K on cooling.

The Synchrotron PXRD data at 300 K were analyzed by Rietveld refinement using the FullProf program [32] using the peak shape function of Thompson-Cox-Hastings Pseudo Voigt convoluted with axial divergence asymmetry and a linear interpolated background. Due to the small amount of Ag dopants in $(Zn_{1-x}Ag_x)_4Sb_3$, the Ag atom was not introduced at each Zn site in the structural

refinement. From the refinement results, the values of the lattice parameters, weight fractions of crystallographic phases existing in the samples, and atomic displacement parameters (ADPs) were obtained. The refinement details are shown in Table S1 in the Supporting Information (SI).

2.3 Potential Seebeck Microprobe scanning

The $(Zn_{1-x}Ag_x)_4Sb_3$ pellets were cut into two halves along the direction perpendicular to the pellet surface after all the high-temperature property measurements, and then the cross section of one half was scanned by a Potential Seebeck Microprobe (PSM II) from PANCO [33]. Each sample was sandwiched by two nickel pieces in order for the microprobe tip to scan the cross-section along the whole width of the sample.

2.4 Thermoelectric properties

The measurements of high-temperature electrical resistivities and Hall coefficients (from room temperature to 575 K in the heating rate of 100 K/h) were carried out under a magnetic field of 1.25 T in a dynamic vacuum on an in-house system [34] using the van der Pauw method. The temperature dependent Seebeck coefficients were measured from room temperature to 575 K in the heating rate of 100 K/h on an in-house uniaxial setup which is similar to the one reported by Iwanaga *et al.* [35]. Due to the bad thermal contact below 373 K, the data of Seebeck coefficient measured in vacuum below 373 K are not reliable for Zn_4Sb_3 samples, we use the cooling data from 575 K to 375 K for analysis. The heating data of Seebeck coefficient measured in vacuum as well as the heating and cooling data of Seebeck coefficient measured in air are shown in Figure S1 in the SI. The densities (d) of the pellets were measured by the Archimedes method with the estimated uncertainty of 2% (shown in Table 1). A Netzsch LFA 457 apparatus was used to measure the thermal diffusivity (D). The results are shown in Figure S2. The heat capacity (C_P) was determined using a reference sample (Pyroceram 9606) in the temperature range 300 – 575 K with steps of 25 K. Then the thermal conductivity was calculated according to the equation $\kappa = DdC_P$. The estimated measurement uncertainties in the values of the electrical resistivity, Seebeck coefficient, and thermal diffusivity are 5%, 5%, and 7%, respectively, and the combined uncertainty for zT is around 20% [36, 37].

2.5 Electron microscopy analysis

A scanning electron microscope (FEI Nova NanoSEM 600) equipped with an energy dispersive spectrometer (EDS) was used to observe the morphology and analyze the elemental distribution by EDS mapping.

2.6 Thermal analysis

Differential Thermal Analysis (DTA) and Thermogravimetry (TG) were conducted in a Netzch STA 449 Jupiter equipped with a TASC414/4 controller. The instrument was calibrated by a standard list. The powders from $(Zn_{1-x}Ag_x)_4Sb_3$ (x = 0, 0.005 and 0.01) samples were loaded into an open alumina crucible. The measurements were performed under the conditions of heating up to 923 K and then cooling down to 303 K with the heating/cooling rate of 10 K/min in Ar atmosphere.

3. Results and discussion

3.1 Crystal structure and XRD characterization

β-Zn_4Sb_3 shows the rhombohedral crystal structure (space group $R\bar{3}c$, as shown in Figure 1) with a = 12.231 Å and c = 12.428 Å. The core structure of β-Zn_4Sb_3 contains three distinct atom sites 36*f* Zn1, 18*e* Sb1, and 12*c* Sb2. 18 Sb^{3-} and 6 Sb_2^{4-} dimers fully occupy 18*e* Sb1 and 12*c* Sb2, respectively. However, the 36*f* Zn1 site is only partially occupied (90%). According to the three-interstitial model, the Zn atoms may randomly occur at the interstitial sites besides the 36*f* Zn1 site (only around 6% occupancy) [38]. The nominal composition of β-Zn_4Sb_3 is $Zn_{13}Sb_{10}$ (or $Zn_{3.9}Sb_3$), and the actual composition of $Zn_{\sim 3.85}Sb_3$ indicating that β-Zn_4Sb_3 is a *p*-type semiconductor.

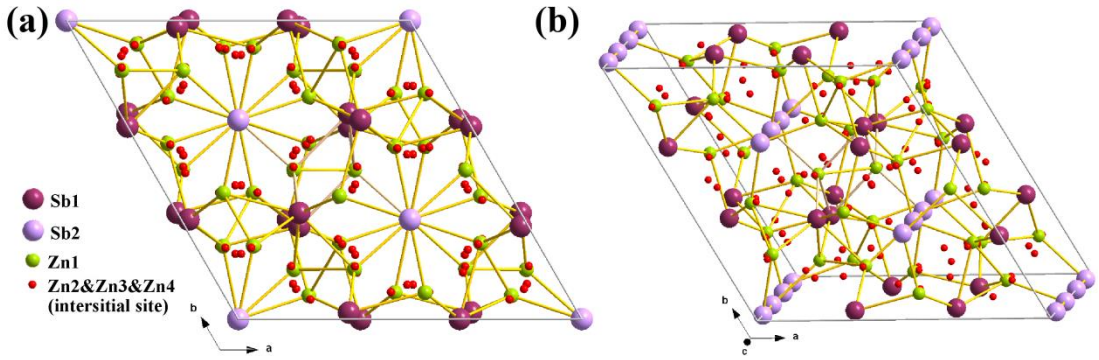

Figure 1. Crystal structure of β-Zn_4Sb_3 with all atomic sites fully occupied.

As seen in Figure 2 (a) and (b), both the top and bottom sides of all the as-synthesized pellets show the main phase of β-Zn_4Sb_3. The additional small reflection Ag_5Zn_8 appear in the Ag-doped samples, and the weak peak reflection from Zn can be seen in the undoped and Ag-doped samples. There is no obvious difference between the top and bottom side, indicating that placing a Zn foil between powders and the bottom punch can compensate the loss of Zn which might migrate along the applied electric current direction, *i.e.* from the bottom side to the top side [29].

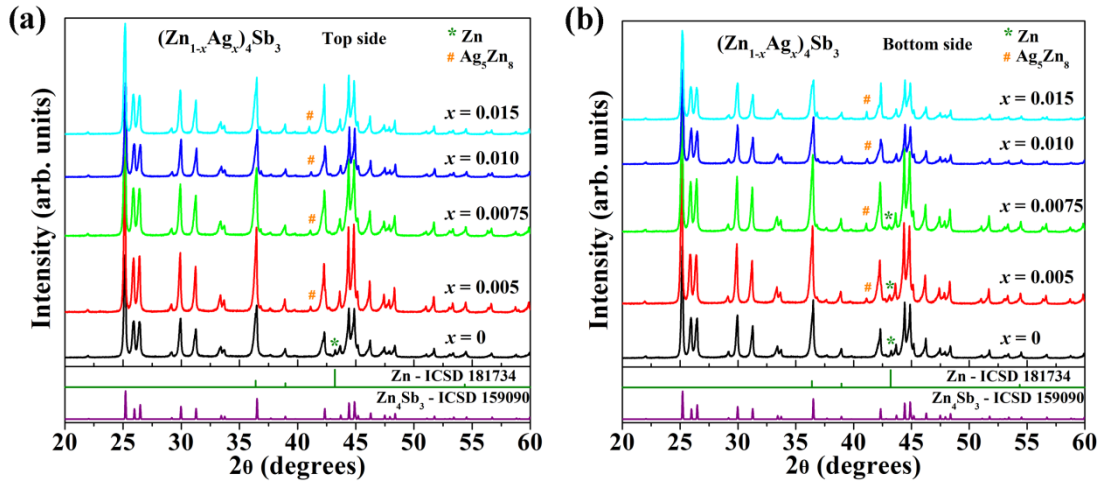

Figure 2. XRD patterns of (a) the top side and (b) the bottom side for the as-pressed $(Zn_{1-x}Ag_x)_4Sb_3$ pellets at room temperature.

3.2 Thermoelectric performance

The as-pressed $(Zn_{1-x}Ag_x)_4Sb_3$ pellets were annealed by running the resistivity measurements from room temperature to 575 K for 3 cycles (Figure S3). For all the samples, after the first cycle the electrical resistivity data show the same temperature dependence trend in the following two cycles due to the annealing effect. The cooling curve of the temperature dependent electrical resistivity in the third cycle for $(Zn_{1-x}Ag_x)_4Sb_3$ samples is shown in Figure 3(a). The electrical resistivity of all the samples increases with increasing the temperature, showing a metallic behavior in the entire temperature range measured. With the increasing Ag content, the resistivity decreases continually from 2.28 to 1.40 mΩ·cm at 300 K as the Ag content *x* increases from 0 to 0.015. This phenomenon is mainly attributed to the increase of the Hall carrier concentration (as seen in Table 1), owing to the fact that Ag^+ has fewer valence electrons than Zn^{2+}. But Ag doping has no obvious effects on the Hall mobility. The Seebeck coefficient of $(Zn_{1-x}Ag_x)_4Sb_3$ samples obtained in the cooling procedure from 575 K to 375 K is shown in Figure 3(b). The positive values of Seebeck coefficient in all the samples indicate that the major carriers are holes, *i.e.* p-type conduction. As the Ag doping content *x* increases from 0 to 0.0075, the Seebeck coefficient increases from 131.8 to 162.2 μV/K at 375 K. But when the silver doping level *x* is higher than 0.0075, the Seebeck coefficient starts to decrease.

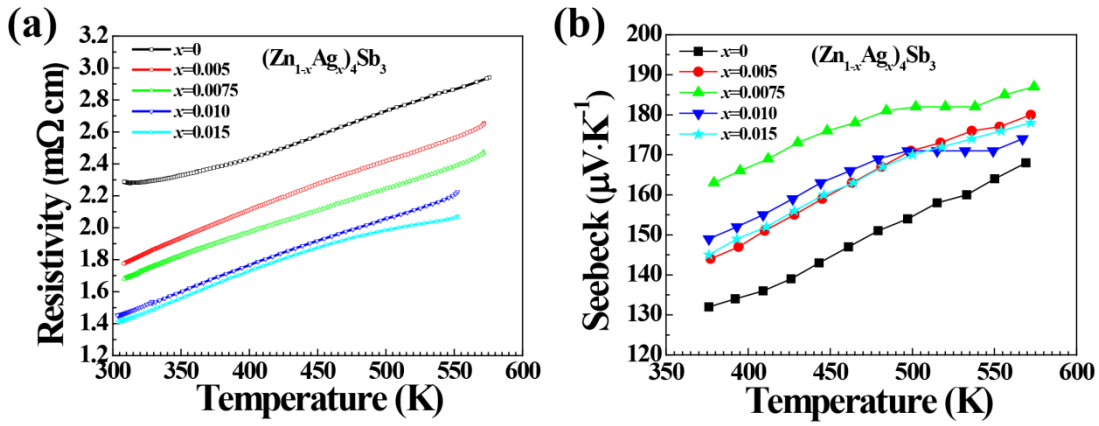

Figure 3. Temperature dependence of (a) electrical resistivity for the cooling segment of the third cycle and (b) Seebeck coefficient for $(Zn_{1-x}Ag_x)_4Sb_3$ pellets for the cooling segment.

Table 1. Room temperature Hall carrier concentration, Hall mobility and the density of $(Zn_{1-x}Ag_x)_4Sb_3$ (*x*=0, 0.005, 0.0075, 0.010, 0.015). The relative density is calculated using the theoretical density of 6.37 g cm^{-3} [4].

Composition	p_H (10^{19} cm^{-3})	μ_H ($cm^2V^{-1}s^{-1}$)	Density (g cm^{-3})	Relative density (%)
Zn_4Sb_3	6.61	40.49	6.23	97.8
$(Zn_{0.995}Ag_{0.005})_4Sb_3$	9.49	37.62	6.25	98.1
$(Zn_{0.9925}Ag_{0.0075})_4Sb_3$	11.60	36.18	6.29	98.7
$(Zn_{0.99}Ag_{0.01})_4Sb_3$	14.23	34.06	6.22	97.6
$(Zn_{0.985}Ag_{0.015})_4Sb_3$	11.33	41.15	6.15	96.5

The calculated power factor (PF = $S^2\sigma$) as a function of temperature for $(Zn_{1-x}Ag_x)_4Sb_3$ samples is shown in Figure 4(a). The magnitude of PF obviously increases from 7.31 to 13.85 μW·cm^{-1}·K^{-2} at 375 K as the Ag content increases from 0 to 0.0075, but decreases slightly as *x* is

above 0.0075. From Figure 4(b), it can be seen that the total thermal conductivity of all the samples show a decreasing trend as the temperature increases. The Ag-doped samples exhibit slightly higher total thermal conductivity than the undoped sample and the total thermal conductivity increases slightly when *x* increases. Owing to the large enhancement of the power factor in the Ag-doped samples, the *zT* values of the Ag-doped samples are obviously higher than that of the undoped sample (shown in Figure 4(c)). The *zT* value increases as *x* increases from 0 to 0.0075 and then decreases as *x* is larger than 0.0075. The highest *zT* value obtained at 575 K is 1.19 for $(Zn_{0.9925}Ag_{0.0075})_4Sb_3$, which is about 28% higher than that of the undoped Zn_4Sb_3 (0.93 at 575 K). As can be seen in Figure 4(d), $Ag_{0.02}Zn_4Sb_3$ reported in reference [39] shows relatively poor thermoelectric performance. For the other state-of-art doped Zn_4Sb_3 samples reported before, most dopants chosen are either toxic (Cd [9], Pb [24]) or expensive rare-earth elements (Pr [40], Sm [41], Gd [42]) to enhance the thermopower through resonant distortion of electronic density of states (DOS). Due to Ge [43] and Nb [13] dopants are sensitive to oxygen the experimental operation should be done in the glove box. Thus, these elements are not ideal chemical dopants for the industrial scaling application. Moreover, these doped Zn_4Sb_3 samples reported do not show better thermoelectric performance than the Ag-doped sample $(Zn_{0.9925}Ag_{0.0075})_4Sb_3$ in our work. The thermoelectric figure of merit *zT* for the best-performing Ag-doped sample $(Zn_{0.9925}Ag_{0.0075})_4Sb_3$ is obviously higher than other state-of-art doped Zn_4Sb_3 materials in the temperature range of 375 - 575 K.

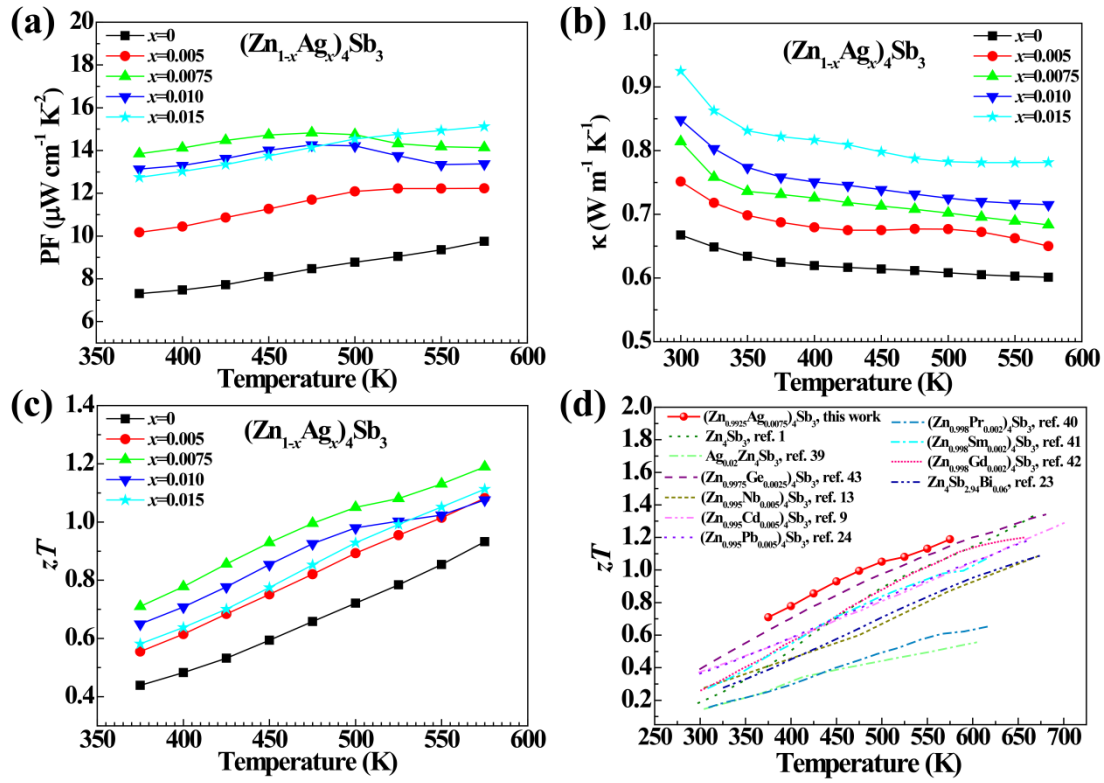

Figure 4. Temperature dependence of the (a) power factor, (b) total thermal conductivity, (c) *zT* value for $(Zn_{1-x}Ag_x)_4Sb_3$ pellets and (d) The temperature dependent *zT* for the best-performing sample $(Zn_{0.9925}Ag_{0.0075})_4Sb_3$. The data of high-temperature *zT* values of other Zn_4Sb_3-based compounds [1, 9, 13, 23, 24, 39-43] are plotted for comparison.

3.3 Thermal stability

3.3.1 Thermal stability of the bulk samples $(Zn_{1-x}Ag_x)_4Sb_3$

After the high-temperature measurements of thermoelectric properties in vacuum, XRD patterns of the top sides of the $(Zn_{1-x}Ag_x)_4Sb_3$ (x = 0, 0.005, 0.0075, 0.01 and 0.015) pellets were measured and shown in Figure 5(a). As can be seen in Figure 5(a), the $(Zn_{1-x}Ag_x)_4Sb_3$ (x = 0, 0.005 and 0.0075) samples still possess Zn_4Sb_3 as the main phase, but there is ZnSb phase appearing on the top surface of the two Ag-doped samples with higher Ag doping levels (x = 0.01 and 0.015), suggesting that Zn can evaporate from the surface of the samples [44] and the decomposition of Zn_4Sb_3 takes place after several temperature dependent measurements cycles (up to 575 K) measurements. However, after polishing the top sides of these two pellets, it is found that Zn_4Sb_3 is still the main phase as seen in Figure 5(b). Moreover, from the PSM scanning images of the cross sections of these two samples (see Figure S4), we can see there is no ZnSb phase which has a Seebeck coefficient distribution around 200 μV/K in the main body. Therefore, it suggests that $(Zn_{1-x}Ag_x)_4Sb_3$ bulk samples show the decomposition of Zn_4Sb_3 only on the surface, and the inner part is stable. Thus, the overall thermoelectric performance would be maintained.

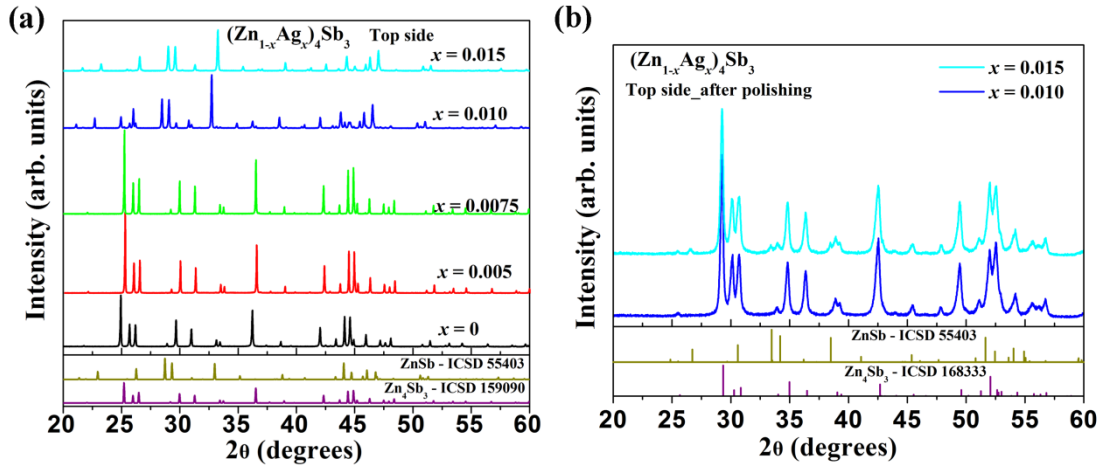

Figure 5. (a) Room temperature XRD (the wavelength: 1.54056 Å) patterns of the top sides of $(Zn_{1-x}Ag_x)_4Sb_3$ (x = 0, 0.005, 0.0075, 0.01 and 0.015) pellets after the property measurements. (b) Room temperature XRD (the wavelength: 1.78892 Å) patterns of the top sides after being polished more for $(Zn_{1-x}Ag_x)_4Sb_3$ (x = 0.01 and 0.015) pellets.

Figure 6 shows the multi-temperature XRD patterns of the top side of the best-performing pellet $(Zn_{0.9925}Ag_{0.0075})_4Sb_3$ in vacuum. Zn_4Sb_3 continues to exist as the main phase apart from a small fraction of the impurity Ag_5Zn_8 as shown in Figure 6(a). The weak diffraction peak of ZnSb appears when the sample was cooled to 301 K in the second cycle, but it disappears as the temperature increases to 793 K in the third cycle, which can be seen more clearly from Figure 6(b). All in all, there is no serious decomposition of Zn_4Sb_3 for the bulk sample in vacuum.

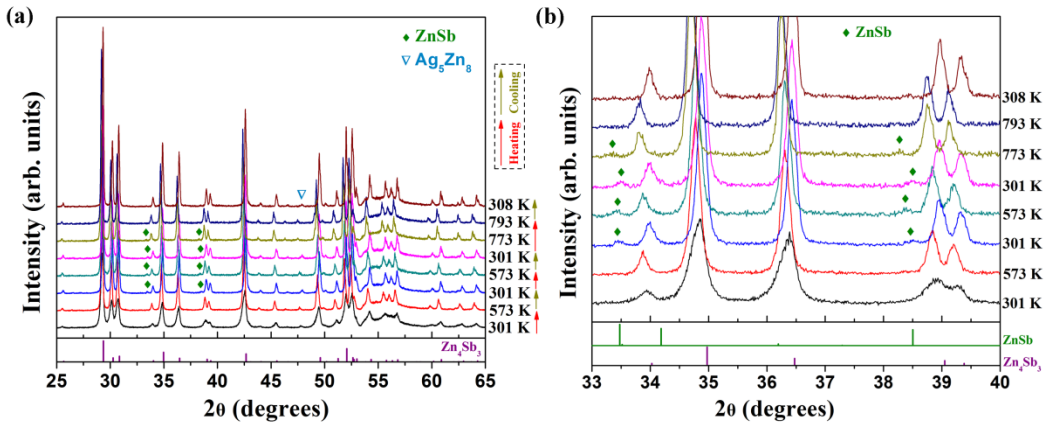

Figure 6. Muti-temperature XRD patterns (Wavelength: 1.78892 Å) of the top side of $(Zn_{0.9925}Ag_{0.0075})_4Sb_3$ pellet between the 2θ range: (a) 25 - 65° and (b) 33 - 40°.

In order to investigate the thermal stability of the bulk samples in air, undoped Zn_4Sb_3 and $(Zn_{0.9925}Ag_{0.0075})_4Sb_3$ samples were both characterized by insitu XRD measurements. The results shown in Figure 7 reveal that there are Zn whiskers coming out of the surface on the two edges for the undoped Zn_4Sb_3 bulk sample, which is in agreement with the observation reported by Hung *et al*. [45]. However, no Zn whisker is observed for the $(Zn_{0.9925}Ag_{0.0075})_4Sb_3$ bulk sample. Figure 8(a) shows the morphology of Zn whiskers which are confirmed by the SEM-EDS elemental mapping images in Figure 8(b). Therefore, the undoped Zn_4Sb_3 bulk sample is unstable in air but the Ag-doped bulk sample is stable in air when the maximum temperature is 573 K.

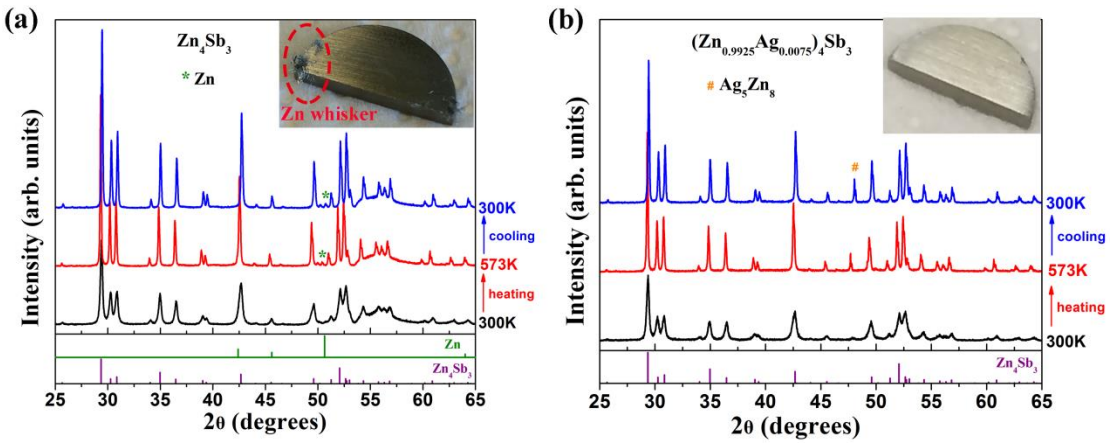

Figure 7. Multi-temperature XRD patterns of the top side of $(Zn_{1-x}Ag_x)_4Sb_3$ pellets in air: (a) x = 0 and (b) x = 0.0075. The insets show the top side of the pellets after multi-temperature XRD measurements in air.

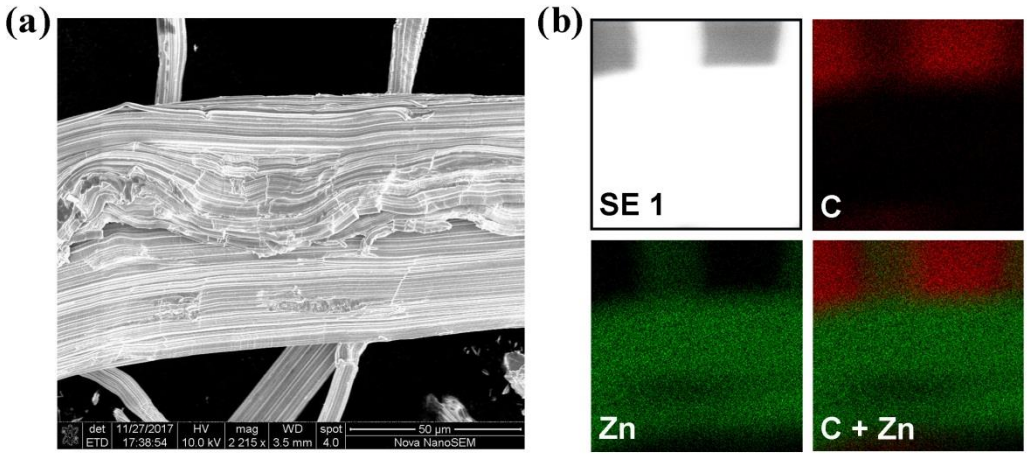

Figure 8. SEM image of Zn whiskers and (b) SEM-EDS elemental mapping images of Zn whiskers on carbon paste.

3.3.2 Thermal stability of the powder samples $(Zn_{1-x}Ag_x)_4Sb_3$

In situ PXRD of pure β-Zn_4Sb_3 is characterized and shown in Figure 9. The powder sample shows pure β-Zn_4Sb_3 phase at room temperature, and ZnSb phase appears at around 473 K. As the temperature increases, the amount of ZnSb phase gradually increases. After the temperature goes up to 773 K and stays at this temperature for 1 h, ZnSb emerges as the main phase and only a small amount of β-Zn_4Sb_3 phase remains in the powder sample. In view of the above results, we can see that β-Zn_4Sb_3 phase in the powder sample could only be stable below 473 K in air, and it starts to decompose into ZnSb and Zn which is oxidized by O_2 to ZnO. This phenomenon is consistent with the instability reported by Iversen *et al*. [26] and Mozharivskyj *et al*. [3].

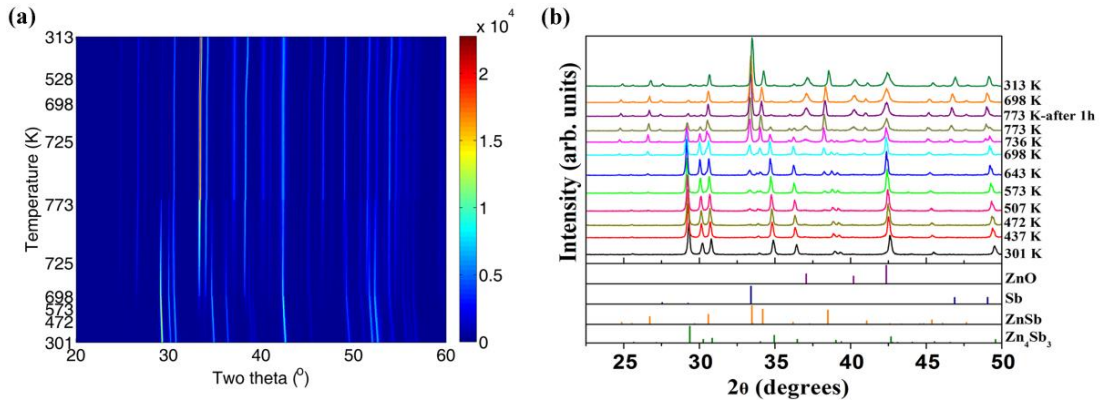

Figure 9. In situ powder XRD patterns of Zn_4Sb_3 powder sample: (a) temperature vs. 2θ and (b) peak intensity vs. 2θ at certain temperatures.

Thermal stability of $(Zn_{1-x}Ag_x)_4Sb_3$ (x = 0, 0.005 and 0.01) powder samples was further investigated by DTA, as shown in Figure 10. In the heating process, the second strongest endothermic peak (x = 0: at 767 K; x = 0.005: at 764 K; x = 0.01: at 769 K) corresponds to the peritectoid reaction from β-Zn_4Sb_3 to γ-Zn_4Sb_3 + ζ-Zn_3Sb_2 phases, the weak peak (x = 0: at 798 K; x = 0.005: at 799 K; x = 0.01: at 804 K) corresponds to the phase transition from γ-Zn_4Sb_3 to γ'-Zn_4Sb_3, and the strongest peak (x = 0 & 0.005: at 839 K; x = 0.01: at 847 K) corresponds to the

melting point of γ'-Zn_4Sb_3 [46]. The two phases (γ- and γ'-Zn_4Sb_3) could be α- and β-$Zn_{9-\delta}Sb_7$, respectively [47]. The other two weak peaks at 745 K and 783 K are also present in the sample with x = 0.01, which could be due to the impurity of Ag-Zn compound. When cooling down from 923 K, the first exothermic peak (x = 0: at 823 K; x = 0.005: at 827 K; x = 0.01: at 828 K) corresponds to the crystallization of ZnSb phase because Zn_4Sb_3 has decomposed into ZnSb and Zn. The two peaks (at 790 K and 748 K for sample x = 0.005; at 792 K and 752 K for sample x = 0) only exist in two samples with x = 0 & 0.005, corresponding to the crystallization of Sb and Zn, respectively, which indicates that some of ZnSb decompose into Zn and Sb. The peak at around 780 K forming in the two Ag-doped samples corresponds to the eutectic reaction transition from liquid to a mixture of two solid phases ZnSb and Sb. The peak at 719 K for the sample x = 0.01 may be identified as the crystallization of ζ-Zn_3Sb_2 phase. The results of DTA in Ar suggest that further decomposition of ZnSb can be inhibited by Ag doping.

Additionally, for the undoped sample, there is no endothermic peak in the heating curve of DTA and no mass loss step in the heating curve of TG (Figure S5) before the peritectoid reaction at 767 K, indicating no decomposition of β-Zn_4Sb_3 below 767 K. However, as the results of in-situ PXRD in air using the same heating/cooling rate show the appearance of ZnSb below 767 K due to the decomposition of β-Zn_4Sb_3 into ZnSb and Zn. Zn can react with the oxygen in air and the decrease in the amount of Zn will speed up the decomposition process [26]. Therefore, we can infer that different ambient atmospheres have different influences on the thermal phase stability of β-Zn_4Sb_3, which agrees with the previous report by Yin *et al*. [27].

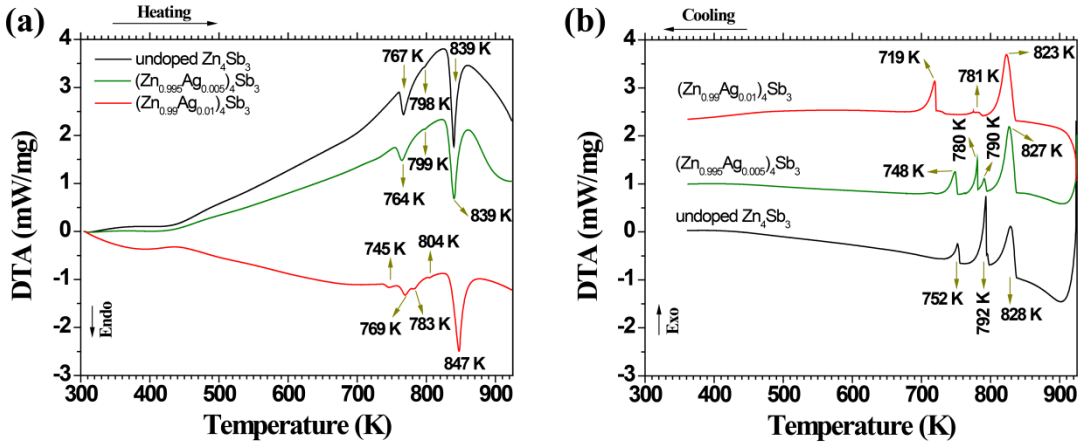

Figure 10. DTA curves of the (a) heating and (b) cooling process for $(Zn_{1-x}Ag_x)_4Sb_3$ (x = 0, 0.005, 0.01) powder samples.

High resolution synchrotron XRD data were also collected for structural analysis of the $(Zn_{1-x}Ag_x)_4Sb_3$ powder samples. The multi-temperature XRD patterns for the undoped Zn_4Sb_3 sample are shown in Figure 11(a). At 300 K before heating, the main phase is Zn_4Sb_3 and there is a small amount of impurities of ZnO and Sb. As seen in Figure 11(b), the observed profile is well described by the calculated profile after the refinement with three phases: Zn_4Sb_3, ZnO and Sb. The detailed refinement results for the XRD data at 300 K from all the three samples are shown in Table S2. As is the case with the undoped sample, the two Ag-doped samples also exhibit the main phase Zn_4Sb_3 which occupies a weight fraction of above 90%.

As depicted in Figure 11(a), when the undoped Zn_4Sb_3 sample was heated up to 773 K,

Zn_4Sb_3 decomposes into ZnSb and Zn, and Zn is then oxidized to ZnO due to the existence of oxygen in the capillary. When the temperature is increased to 793 K, most of ZnSb decompose. After cooling back to 300 K, only around 10% of ZnSb remain in the sample, and the weight fractions of Sb and ZnO phases are 45.03(20)% and 44.88(15)%, respectively.

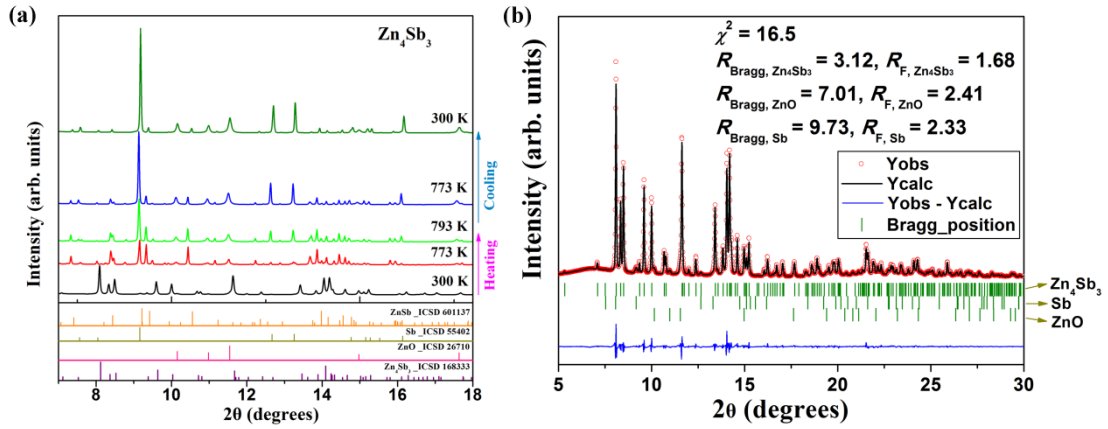

Figure 11. (a) Multi-temperature synchrotron X-ray diffraction patterns for undoped Zn_4Sb_3, (b) the calculated and observed diffraction patterns at 300 K before heating.

Figure 12(a) and 12(b) show the multi-temperature synchrotron XRD patterns for the two Ag-doped samples. The decomposition of Zn_4Sb_3 phase into ZnSb also takes place for both Ag-doped samples when the temperature is increased to 773 K. However, after the two Ag-doped powder samples were cooled down from 793 K to 300 K, there is still Zn_4Sb_3 remaining (23.89(16)% for x = 0.005 and 6.29(7)% for x = 0.01. ZnSb phase is the main phase after cooling down to 300 K. There are 67.61(24)% and 76.92(18)% of ZnSb for x = 0.005 & 0.01, respectively. It is worth mentioning that ZnSb shows good thermoelectric performance which can be further improved by Ag doping [48], thus the thermoelectric performance of Ag doped Zn_4Sb_3 material at high temperatures up to 793 K can stay at a good level. The results clearly indicate Ag doping can improve the high-temperature thermal stability of Zn_4Sb_3 material and also inhibit the further phase decomposition of ZnSb.

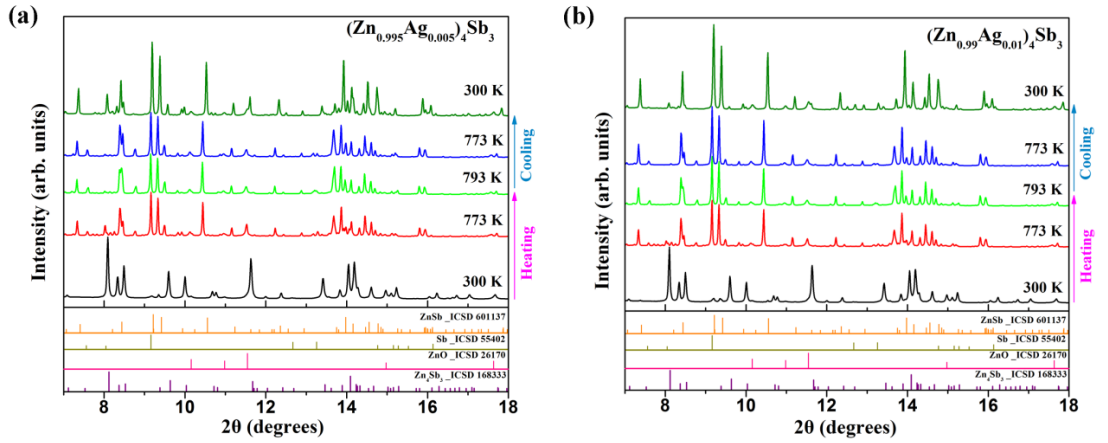

Figure 12. Multi-temperature synchrotron X-ray diffraction patterns for $(Zn_{1-x}Ag_x)_4Sb_3$: (a) x = 0.005 and (b) x = 0.01.

4. Conclusion

The thermoelectric properties at 300 - 575 K and high-temperature thermal stability of $(Zn_{1-x}Ag_x)_4Sb_3$, which were synthesized by the direct spark plasma sintering method, were investigated in this work. Ag doping at the Zn sites can enhance the thermoelectric performance with the highest zT value of ~1.2 at 575 K for the $(Zn_{0.9925}Ag_{0.0075})_4Sb_3$ bulk sample, and importantly the $(Zn_{0.9925}Ag_{0.0075})_4Sb_3$ bulk sample is stable when it was heated up to 793 K under vacuum and also stable when the temperature is elevated to 573 K in air. Combining In-house in situ powder X-ray diffraction (PXRD) and multi-temperature synchrotron PXRD (up to 793 K), we found that Ag doping stabilizes Zn_4Sb_3 to avoid the decomposition into ZnSb and the further decomposition of ZnSb into Sb is also inhibited when the temperature goes up to 793 K and down to 300 K. In conclusion, Ag-doped Zn_4Sb_3 bulk materials still could be a promising thermoelectric material for intermediate temperature range applications.

Acknowledgements

This study was supported by the Danish National research Foundation (Center for Materials Crystallography, DNRF93) and the Innovation Foundation of Denmark (Center for Thermoelectric Energy Conversion), and the Danish Center for Synchrotron and Neutron Research (Danscatt). The authors would like to thank the synchrotron beamlines BL02B2 (Proposal No. 2016A0074) and RIKEN BL44B2 (Proposal No. 20160037) at SPring-8 for the beamtime allocation. ABB gratefully acknowledges financial support from The Research Council of Norway under the Toppforsk program to the project (No 250403) “From Aqueous Solutions to Oxide Thin Films and Hierarchica Structures”.

References

[1] T. Caillat, J.P. Fleurial, A. Borshchevsky, Preparation and thermoelectric properties of semiconducting Zn_4Sb_3, J. Phys. Chem. Solids, 58 (1997) 1119-1125.

[2] Y. Mozharivskyj, Y. Janssen, J.L. Harringa, A. Kracher, A.O. Tsokol, G.J. Miller, $Zn_{13}Sb_{10}$: A structural and Landau theoretical analysis of its phase transitions, Chem. Mater., 18 (2006) 822-831.

[3] Y. Mozharivskyj, A.O. Pecharsky, S. Bud'ko, G.J. Miller, A promising thermoelectric material: Zn_4Sb_3 or $Zn_{6-\delta}Sb_5$. Its composition, structure, stability, and polymorphs. Structure and stability of $Zn_{1-\delta}Sb$, Chem. Mater., 16 (2004) 1580-1589.

[4] G.J. Snyder, M. Christensen, E. Nishibori, T. Caillat, B.B. Iversen, Disordered zinc in Zn_4Sb_3 with phonon-glass and electron-crystal thermoelectric properties, Nat. Mater., 3 (2004) 458-463.

[5] F. Cargnoni, E. Nishibori, P. Rabiller, L. Bertini, G.J. Snyder, M. Christensen, C. Gatti, B.B. Iversen, Interstitial Zn atoms do the trick in thermoelectric zinc antimonide, Zn_4Sb_3: A combined maximum entropy method X-ray electron density and ab initio electronic structure study, Chem.-Eur. J., 10 (2004) 3861-3870.

[6] L. Bjerg, B.B. Iversen, G.K.H. Madsen, Modeling the thermal conductivities of the zinc antimonides ZnSb and Zn_4Sb_3, Phys. Rev. B, 89 (2014).

[7] S.C. Ur, P. Nash, I.H. Kim, Mechanical alloying and thermoelectric properties of Zn_4Sb_3, J. Mater. Sci., 38 (2003) 3553-3558.

[8] T.H. Zou, X.Y. Qin, D. Li, G.L. Sun, Y.C. Dou, Q.Q. Wang, B.J. Ren, J. Zhang, H.X. Xin, Y.Y. Li, Simultaneous enhancement in thermoelectric power factor and phonon blocking in hierarchical nanostructured beta-Zn_4Sb_3-Cu_3SbSe_4, Appl. Phys. Lett., 104 (2014).
[9] S.Y. Wang, H. Li, D.K. Qi, W.J. Xie, X.F. Tang, Enhancement of the thermoelectric performance of beta-Zn_4Sb_3 by in situ nanostructures and minute Cd-doping, Acta Mater., 59 (2011) 4805-4817.
[10] F. Liu, X.Y. Qin, H.X. Xin, Thermoelectric properties of $(Zn_{0.98}M_{0.02})_4Sb_3$ (M=Al, Ga and In) at low temperatures, J. Phys. D: Appl. Phys., 40 (2007) 7811-7816.
[11] H.J. Gau, J.L. Yu, C.C. Wu, Y.K. Kuo, C.H. Ho, Thermoelectric properties of Zn-Sb alloys doped with In, J. Alloys Compd., 480 (2009) 73-75.
[12] B.L. Pedersen, H. Birkedal, E. Nishibori, A. Bentien, M. Sakata, M. Nygren, P.T. Frederiksen, B.B. Iversen, $Hg_{0.04}Zn_{3.96}Sb_3$: Synthesis, crystal structure, phase transition, and thermoelectric properties, Chem. Mater., 19 (2007) 6304-6311.
[13] D. Li, H.H. Hng, J. Ma, X.Y. Qin, Effects of Nb doping on thermoelectric properties of Zn_4Sb_3 at high temperatures, J. Mater. Res., 24 (2009) 430-435.
[14] W. Li, L.M. Zhou, Y.L. Li, J. Jiang, G.J. Xu, Thermoelectric properties of hot-pressed $Zn_4Sb_{3-x}Te_x$, J. Alloys Compd., 486 (2009) 335-337.
[15] D. Li, X.Y. Qin, Effects of Te doping on the transport and thermoelectric properties of Zn_4Sb_3, Intermetallics, 19 (2011) 1651-1655.
[16] B.L. Pedersen, H. Birkedal, M. Nygren, P.T. Frederiksen, B.B. Iversen, The effect of Mg doping on the thermoelectric performance of Zn_4Sb_3, J. Appl. Phys., 105 (2009).
[17] H. Yin, B.B. Iversen, Effect of Mg-Doping on the Thermal Stability of Thermoelectric Zn_4Sb_3, Sci. Adv. Mater., 3 (2011) 592-595.
[18] M.A. Liu, X.Y. Qin, C.S. Liu, L. Pan, H.X. Xin, Ag and Cu doping and their effects on the thermoelectric properties of beta-Zn_4Sb_3, Phys. Rev. B, 81 (2010).
[19] L. Pan, X.Y. Qin, M. Liu, F. Liu, Effects of Ag doping on thermoelectric properties of Zn_4Sb_3 at low temperatures, J. Alloys Compd., 489 (2010) 228-232.
[20] L. Pan, X.Y. Qin, M. Liu, The effects of iodine doping on the thermoelectric properties of Zn_4Sb_3 at low temperatures, Solid State Commun., 150 (2010) 346-349.
[21] L. Pan, X.Y. Qin, M. Liu, Effects of Se doping on thermoelectric properties of Zn_4Sb_3 at low-temperatures, Solid State Sci., 12 (2010) 257-261.
[22] L. Pan, X.Y. Qin, H.X. Xin, D. Li, J.H. Sun, J. Zhang, C.J. Song, R.R. Sun, Enhanced thermoelectric properties of iron doped compound $(Zn_{1-x}Fe_x)_4Sb_3$, Intermetallics, 18 (2010) 1106-1110.
[23] L.M. Zhou, W. Li, J. Jiang, T. Zhang, Y. Li, G.J. Xu, P. Cui, Effect of Bi doping on the thermoelectric properties of Zn_4Sb_3, J. Alloys Compd., 503 (2010) 464-467.
[24] S.Y. Wang, X.Y. She, G. Zheng, F. Fu, H. Li, X.F. Tang, Enhanced Thermoelectric Performance and Thermal Stability in beta-Zn_4Sb_3 by Slight Pb-Doping, J. Elec. Mater., 41 (2012) 1091-1099.
[25] B.L. Pedersen, H. Birkedal, P.T. Frederiksen, B.B. Iversen, High temperature stability of thermoelectric Zn_4Sb_3, Proc. 25th Inter. Conf. on Thermoelectrics, (2006) 520-523.
[26] B.B. Iversen, Fulfilling thermoelectric promises: beta-Zn_4Sb_3 from materials research to power generation, J. Mater. Chem., 20 (2010) 10778-10787.
[27] H. Yin, M. Christensen, B.L. Pedersen, E. Nishibori, S. Aoyagi, B.B. Iversen, Thermal Stability of Thermoelectric Zn_4Sb_3, J. Elec. Mater., 39 (2010) 1957-1959.
[28] H. Yin, B.L. Pedersen, B.B. Iversen, Thermal Stability of High Performance Thermoelectric beta-Zn_4Sb_3 in Argon, Eur. J. Inorg. Chem., (2011) 2733-2737.

[29] H. Yin, A.B. Blichfeld, M. Christensen, B.B. Iversen, Fast Direct Synthesis and Compaction of Homogenous Phase-Pure Thermoelectric Zn_4Sb_3, Acs Appl. Mater. Inter., 6 (2014) 10542-10548.
[30] E. Nishibori, M. Takata, K. Kato, M. Sakata, Y. Kubota, S. Aoyagi, Y. Kuroiwa, M. Yamakata, N. Ikeda, The large Debye-Scherrer camera installed at SPring-8 BL02B2 for charge density studies, Nucl. Instr. Meth. Phys. Res. A, 467 (2001) 1045-1048.
[31] K. Kato, R. Hirose, M. Takemoto, S. Ha, J. Kim, M. Higuchi, R. Matsuda, S. Kitagawa, M. Takata, The RIKEN Materials Science Beamline at SPring-8: Towards Visualization of Electrostatic Interaction, AIP Conf. Proc. 1234 (2010) 875-878.
[32] J. Rodríguez-Carvajal, Recent advances in magnetic structure determination by neutron powder diffraction, Phys. B: Condens. Matter, 192 (1993) 55-69.
[33] D. Platzek, G. Karpinski, C. Stiewe, P. Ziolkowski, C. Drasar, E. Muller, Potential-Seebeck-Microprobe (PSM): Measuring the spatial resolution of the Seebeck coefficient and the electric potential, Proc. 24th Inter. Conf. on Thermoelectrics, (2005) 13-16.
[34] K.A. Borup, E.S. Toberer, L.D. Zoltan, G. Nakatsukasa, M. Errico, J.-P. Fleurial, B.B. Iversen, G.J. Snyder, Measurement of the electrical resistivity and Hall coefficient at high temperatures, Rev. Sci. Instrum., 83 (2012) 123902.
[35] S. Iwanaga, E.S. Toberer, A. LaLonde, G.J. Snyder, A high temperature apparatus for measurement of the Seebeck coefficient, Rev. Sci. Instrum., 82 (2011) 063905.
[36] H. Wang, W.D. Porter, H. Bottner, J. Konig, L.D. Chen, S.Q. Bai, T.M. Tritt, A. Mayolet, J. Senawiratne, C. Smith, F. Harris, P. Gilbert, J.W. Sharp, J. Lo, H. Kleinke, L. Kiss, Transport Properties of Bulk Thermoelectrics-An International Round-Robin Study, Part I: Seebeck Coefficient and Electrical Resistivity, J. Elec. Mater., 42 (2013) 654-664.
[37] H. Wang, W.D. Porter, H. Bottner, J. Konig, L.D. Chen, S.Q. Bai, T.M. Tritt, A. Mayolet, J. Senawiratne, C. Smith, F. Harris, P. Gilbert, J. Sharp, J. Lo, H. Kleinke, L. Kiss, Transport Properties of Bulk Thermoelectrics: An International Round-Robin Study, Part II: Thermal Diffusivity, Specific Heat, and Thermal Conductivity, J. Elec. Mater., 42 (2013) 1073-1084.
[38] J. Nylen, M. Andersson, S. Lidin, U. Haussermann, The structure of alpha-Zn_4Sb_3: Ordering of the phonon-glass thermoelectric material beta-Zn_4Sb_3, J. Am. Chem. Soc., 126 (2004) 16306-16307.
[39] F.S. Liu, L.C. Pan, W.Q. Ao, L.P. He, X.X. Li, H.T. Li, J.Q. Li, Effect of Addition of Ag, In or Pb on the Structure and Thermoelectric Performance of beta-Zn_4Sb_3, J. Elec. Mater., 41 (2012) 2118-2125.
[40] Q.Q. Wang, X.Y. Qin, D. Li, R.R. Sun, T.H. Zou, N.N. Wang, Resonant distortion of electronic density of states and enhancement of thermoelectric properties of beta-Zn_4Sb_3 by Pr doping, J. Appl. Phys., 113 (2013).
[41] Q.Q. Wang, X.Y. Qin, D. Li, T.H. Zou, Enhancement of thermopower and thermoelectric performance through resonant distortion of electronic density of states of β-Zn_4Sb_3 doped with Sm, Appl. Phys. Lett., 102 (2013).
[42] B.J. Ren, M.A. Liu, X.G. Li, X.Y. Qin, D. Li, T.H. Zou, G.L. Sun, Y.Y. Li, H.X. Xin, J. Zhang, Enhancement of thermoelectric performance of beta-Zn_4Sb_3 through resonant distortion of electronic density of states doped with Gd, J. Mater. Chem. A, 3 (2015) 11768-11772.
[43] S.Y. Wang, X.J. Tan, G.J. Tan, X.Y. She, W. Liu, H. Li, H.J. Liu, X.F. Tang, The realization of a high thermoelectric figure of merit in Ge-substituted beta-Zn_4Sb_3 through band structure modification, J. Mater. Chem., 22 (2012) 13977-13985.
[44] X. Song, M. Schrade, N. Maso, T.G. Finstad, Zn vacancy formation, Zn evaporation and decomposition of ZnSb at elevated temperatures: Influence on the microstructure and the electrical

properties, J. Alloys Compd., 710 (2017) 762-770.
[45] L.T. Hung, D.T. Ngo, L. Han, B.B. Iversen, H. Yin, N. Pryds, V.N. Nong, In Operando Study of High-Performance Thermoelectric Materials for Power Generation: A Case Study of β-Zn_4Sb_3, Adv. Electron. Mater., 3 (2017).
[46] S.C. Ur, I.H. Kim, P. Nash, Thermoelectric properties of Zn_4Sb_3 processed by sintering of cold pressed compacts and hot pressing, J. Mater. Sci., 42 (2007) 2143-2149.
[47] A. He, V. Svitlyk, D. Chernyshov, Y. Mozharivskyj, Identification, structural characterization and transformations of the high-temperature $Zn_{9-\delta}Sb_7$ phase in the Zn-Sb system, Dalton Trans., 44 (2015) 20983-20990.
[48] D.B. Xiong, N.L. Okamoto, H. Inui, Enhanced thermoelectric figure of merit in p-type Ag-doped ZnSb nanostructured with Ag_3Sb, Scripta Mater., 69 (2013) 397-400.

Supporting Information

Table S1. Rietveld refinement details of the synchrotron XRD data at 300 K.
(The R factors and χ^2 shown here are the data from the main phase whose weight fraction value was filled in grey color below)

Parameters		Zn_4Sb_3		$(Zn_{0.995}Ag_{0.005})_4Sb_3$		$(Zn_{0.99}Ag_{0.01})_4Sb_3$	
T(K)		300-1	300-2	300-1	300-2	300-1	300-2
$t_{exp.}$(min)		15	15	15	15	15	15
No. of points		7930	7931	7931	7933	7935	7934
No. of reflections		3241	452	3268	3470	3230	3463
No. of parameters		51	56	56	56	61	63
R_F (%)		1.68	2.37	1.85	2.77	2.90	2.08
R_{Bragg} (%)		3.12	3.51	3.70	5.26	3.20	3.14
R_p (%)		7.70	11.0	7.48	11.6	8.47	8.17
R_{wp} (%)		8.42	12.0	8.07	14.4	9.05	9.19
χ^2		16.5	56.2	16.0	61.3	16.9	25.0
Wt.% Zn_4Sb_3		94.34(0.19)	-	93.09(0.19)	23.89(0.16)	90.81(0.21)	6.29(0.07)
Wt.% ZnO		4.42(0.06)	45.03(0.20)	5.58(0.08)	8.50(0.12)	5.32(0.10)	12.22(0.08)
Wt.% Sb		1.24(0.03)	44.88(0.15)	1.33(0.03)	-	1.02(0.04)	4.56(0.04)
Wt.% ZnSb		-	10.10(0.09)	-	67.61(0.24)	2.85(0.06)	76.92(0.18)
Zn_4Sb_3	a=b(Å)	12.21951(15)	-	12.21970(12)	12.23696(20)	12.20993(17)	12.22394(34)
	c(Å)	12.40562(16)	-	12.40552(13)	12.43208(25)	12.39731(18)	12.41722(47)
	Biso Sb1	0.762(0)	-	0.771(0)	0.625(0)	0.981(0)	0.477(0)
	Biso Sb2	0.792(0)	-	0.752(0)	1.150(0)	0.954(0)	1.050(0)
	Biso Zn1	1.431(0)	-	1.326(0)	1.790(0)	1.324(0)	1.251(0)
	Volume ($Å^3$)	1604.1941	-	1604.2468	1612.2084	1600.5718	1606.8555
ZnSb	a(Å)	-	6.20376(15)	-	6.20334(7)	6.20180(68)	6.19815(5)
	b(Å)	-	7.74261(19)	-	7.74292(9)	7.73406(91)	7.73611(6)
	c(Å)	-	8.09745(19)	-	8.09937(10)	8.09277(114)	8.09145(6)

	Biso Zn1	-	0.455(0)	-	0.957(0)	1.500(0)	1.000(0)
	Biso Sb1	-	0.462(0)	-	0.426(0)	1.280(0)	0.412(0)
	Volume ($Å^3$)	-	388.9665	-	389.0283	388.1897	387.9815

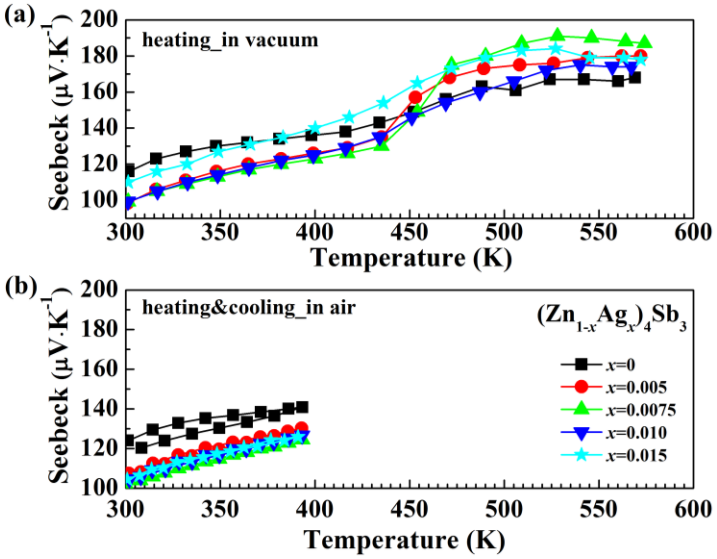

Figure S1. Temperature dependence of Seebeck coefficient for the $(Zn_{1-x}Ag_x)_4Sb_3$ pellets: (a) heating data measured in vacuum and (b) heating & cooling data measured in air.

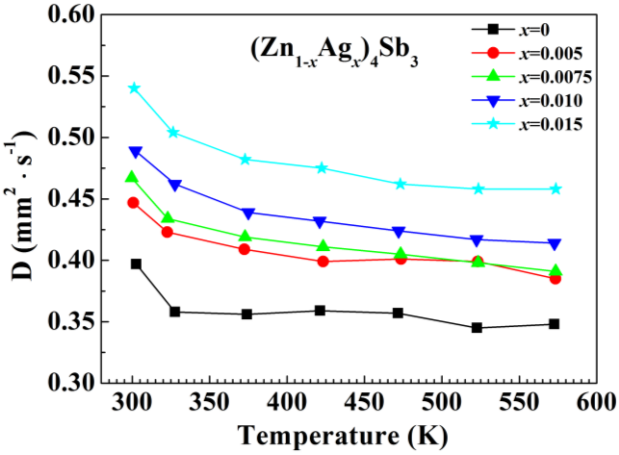

Figure S2. Temperature dependence of thermal diffusivity measured by LFA for the $(Zn_{1-x}Ag_x)_4Sb_3$ pellets.

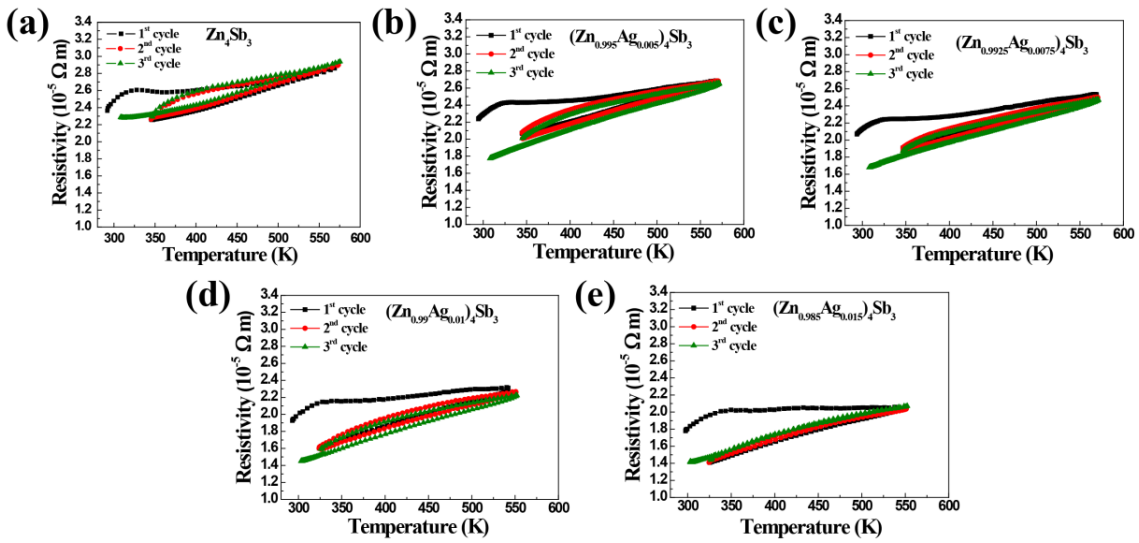

Figure S3. Temperature dependence of the electrical resistivity for the as-pressed $(Zn_{1-x}Ag_x)_4Sb_3$ pellets in three cycles: (a) x = 0, (b) x = 0.005, (c) x = 0.0075, (d) x = 0.01 and (e) x = 0.015.

Figure S3 shows that as the Ag content increases, the hysteresis loop between the heating and cooling curves becomes smaller and even disappears for the sample with x = 0.015, indicating that Ag doing has an influence on the microstructure change of Zn_4Sb_3 while undergoing the heat treatment.

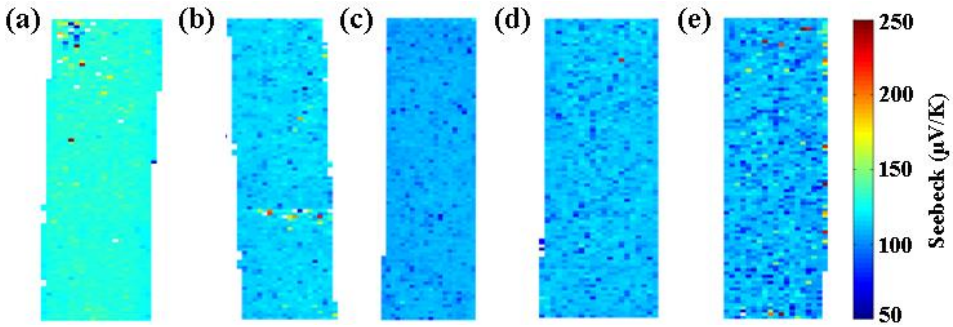

Figure S4. Room temperature PSM scanning images of the cross sections for $(Zn_{1-x}Ag_x)_4Sb_3$ pellets after the property measurements: (a) x = 0, (b) x = 0.005, (c) x = 0.0075, (d) x = 0.01 and (e) x = 0.015.

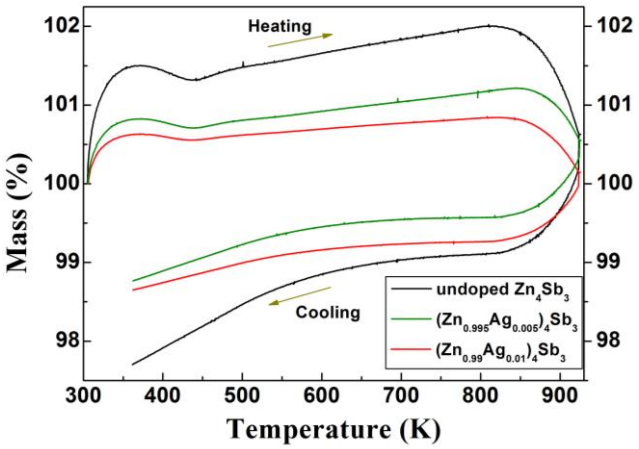

Figure S5. TG curves of the (a) heating and (b) cooling process for $(Zn_{1-x}Ag_x)_4Sb_3$ (x = 0, 0.005, 0.01) powder samples.